Sintering and microstuctural characterization of W^{6+}, Nb^{5+} and Ti^{4+} iron-substituted $BiFeO_3$

M.S. Bernardo*, T. Jardiel, M. Peiteado, A.C. Caballero, M. Villegas

Department of Electroceramics, Instituto de Cerámica y Vidrio, CSIC, 28049 Madrid, Spain

A B S T R A C T

The sintering behaviour and the microstructural evolution of W^{6+}, Nb^{5+} and Ti^{4+} iron-substituted $BiFeO_3$ ceramics have been analyzed. The obtained results show that W^{6+} and Nb^{5+} ions interact with the secondary phases usually present in these materials, thus altering the solid state formation of the $BiFeO_3$ phase. In contrast, Ti^{4+} ions incorporate into the perovskite structure, leading to an exceptionally low proportion of secondary phases. In addition to this, $BiFe_{0,95}Ti_{0,05}O_3$ materials present a dense microstructure with submicronic and nanostructured grains, clearly smaller than those in the undoped materials.

Keywords:
Multiferroic materials
X-ray diffraction
Solid state reactions
Sintering
Scanning electron microscopy
Microstructure

1. Introduction

Multiferroic materials, which exhibit simultaneous ferroelectric, ferromagnetic and ferroelastic order within the same phase, have gained increasing interest in the last few years due to their potential technological applications [1,2]. In particular bismuth ferrite is one of the most promising multiferroics. At room temperature, bulk $BiFeO_3$ presents a rhomboedrally distorted perovskite structure belonging to the space group R3c [3]. It presents considerably high phase transition temperatures which explain the increasing interest for this material; these temperatures are 370 °C for the transition from anti-ferromagnetic to paramagnetic ($T_{Néel}$) and 830 °C for the transition from ferroelectric to paraelectric (T_{Curie}) [3].

However, $BiFeO_3$ materials usually present a high electrical conductivity that hinders its practical applications. This high leakage current is mainly attributed to the presence of secondary phases, namely the Bi-rich sillenite type $Bi_{25}FeO_{39}$ phase and the Fe-rich mullite type $Bi_2Fe_4O_9$ phase, and to defects in the crystal structure, such as oxygen vacancies originated by the reduction of Fe^{3+} to Fe^{2+} [3,4]. Many attempts are being done in order to obtain pure $BiFeO_3$ using methods such as chemical synthesis (including co-precipitation [5], sol–gel [6], polymerizable complex methods [7] and hydrothermal or solvothermal synthesis [8,9]) mechanical activated synthesis [10], micro-wave assisted synthesis [11,12] or rapid-sintering [13]. However, up to date, the obtaining of bismuth ferrite as a pure-single phase product still represents a major challenge. The presence of these undesired phases is commonly attributed to a very narrow range of stabilization of the $BiFeO_3$ phase [14,15] and to the presence of impurities at trace levels that promote the stabilization of secondary phases [16]. These phases are often difficult to detect by X-ray diffraction because the $Bi_{25}FeO_{39}$ sillenite phase is not always well crystallized and, also, because its high proportion of heavy Bi^{3+} ions (which, with 80 electrons, scatters X-rays much more efficiently than the much lighter Fe^{2+} and O^{2-}, with 24 and 10 electrons respectively) disguises the signal of the iron-rich $Bi_2Fe_4O_9$ phase [16]. For this reason, a rigorous microstructural characterization is always essential in order to detect traces of secondary phases.

In the last few years many researches have tried to stabilize the $BiFeO_3$ phase by partial substitution of A or B-site in the perovskite structure [17–20]. Since $BiFeO_3$ is a p-type semiconductor [21], doping with donor dopants will result in a decrease of the electrical conductivity [22]. However, the $BiFeO_3$ structure is more closely packed than that of $Bi_{25}FeO_{39}$ and $Bi_2Fe_4O_9$ secondary phases [15] so it is easy that many dopants interact with the secondary phases instead of the bismuth ferrite. Because of that, doping may result in materials with an even higher proportion of secondary phases [23]. Many papers report changes in the electrical and magnetic properties of $BiFeO_3$-based materials upon doping, but very few

* Corresponding author at: Department of Electroceramics, Instituto de Ceramica y Vidrio, CSIC, C/Kelsen 5, 28049 Madrid, Spain. Tel.: +34 917355840; fax: +34 917355843.
E-mail address: mbernardo@icv.csic.es (M.S. Bernardo).

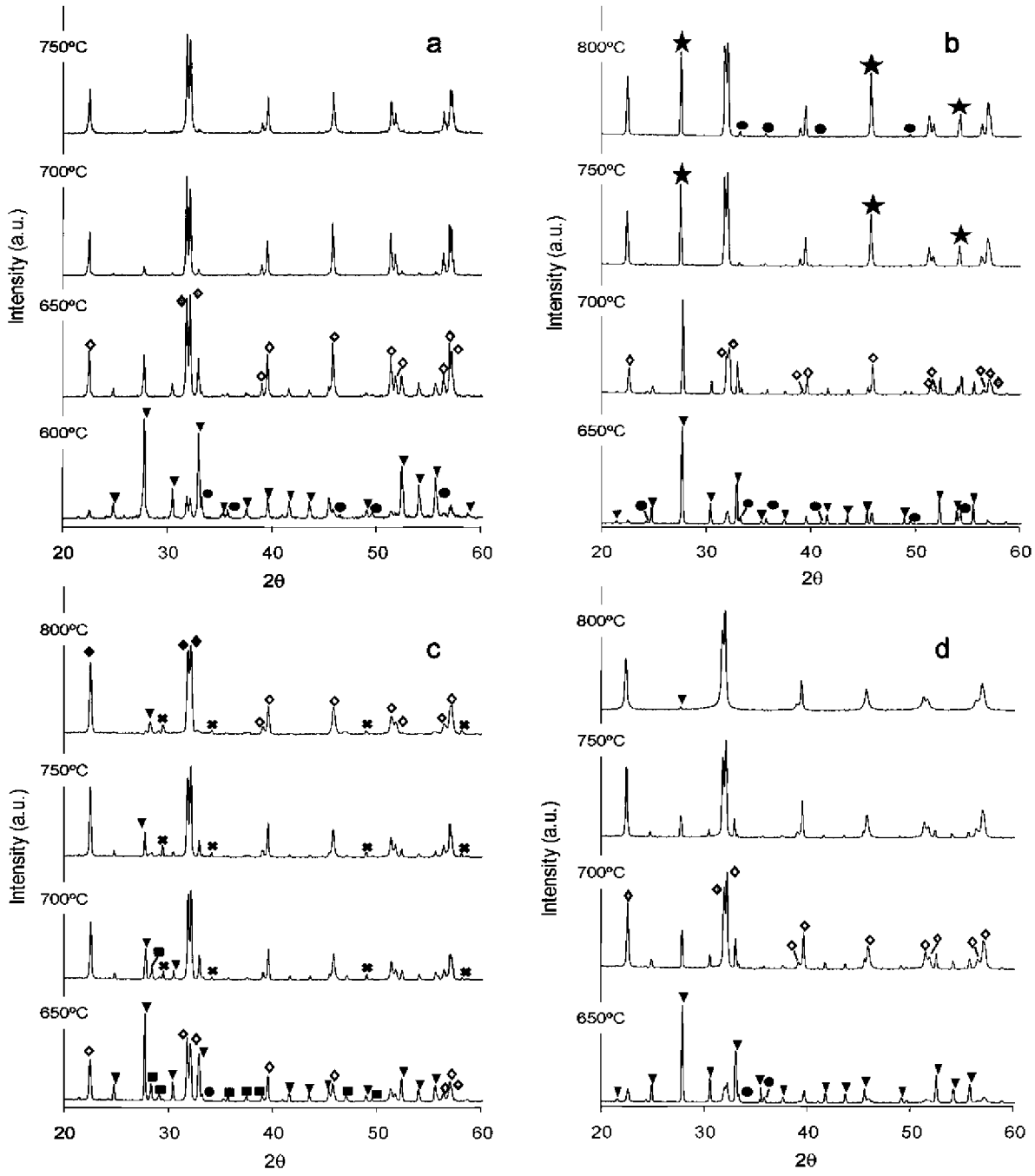

Fig. 1. X-ray diffractograms of the samples corresponding to BF (a), BFW (b), BFN (c) and BFT (d) compositions calcined at different temperatures. $BiFeO_3$ (♦), Fe_2O_3 (●), $Bi_{25}FeO_{39}$ (▼), $Bi_{14}W_2O_{27}$ (⋆), $Bi_2Fe_4O_9$ (■) and the Bi–Nb–Fe–O pyrochlore (✖).

of them thoroughly describe their structural and microstructural changes. In fact, some of the properties reported for $BiFeO_3$ materials are a consequence of the presence of secondary phases, i.e. Azough et al. noticed that the ferromagnetism observed in the CoO- or NiO-added $BiFeO_3$ samples was due to the presence of $CoFe_2O_4$ or $NiFe_2O_4$ nanoparticles rather than to the $BiFeO_3$ matrix phase [24]. As a consequence, results presented in many of these works are frequently contradictory and the question of how to stabilize single-phase $BiFeO_3$ with improved multiferroic behaviour and suitable for practical devices still remains controversial.

Donor dopants like Ti^{4+}, Nb^{5+} and W^{6+} have been suggested to enhance the ferroelectric properties of $BiFeO_3$ [25–32]. In octahedral coordination, their ionic radii (0.605, 0.64 and 0.60 Å respectively) [33] are close to the high spin [34] ionic radii of Fe^{3+} (0.645 Å) [33], hence these ions could easily enter the B-sites of the perovskite lattice. Due to its higher valence state compared to the Fe^{3+}, the substitution should also entail a decrease in the oxygen vacancies concentration [22]. However, the changes that these ions produce in the structure and the microstructure of the $BiFeO_3$ materials are still unknown or not correctly described, and contradictory results are once more found in the literature. Although most of the researchers report an increase in the electrical resistivity upon doping with these ions, the suggested conduction mechanisms and the precise role of each dopant typically differ. For example, Jun

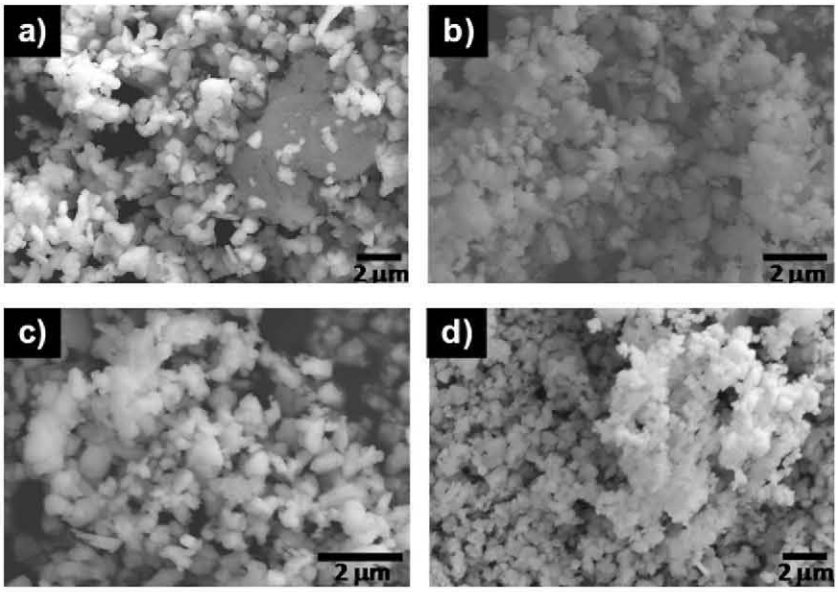

Fig. 2. FE-SEM micrographs of the powders corresponding to the compositions: BF calcined at 750 °C/2 h (a), BFW calcined at 800 °C/2 h (b), BFN calcined at 800 °C/2 h (c) and BFT calcined at 800 °C/2 h (d).

et al. propose that Nb-doping enhances the resistivity of the material through a grain boundary mechanism caused by segregation of the dopant to the $BiFeO_3$ grain boundaries [28,29], whereas Simões et al. suggest that the suppression of oxygen vacancies due to substitution of Fe^{3+} for the higher valence-state ion Nb^{5+} is the reason for the observed reduction in conductivity [30,31]. In this sense the microstructural features are key to determine both the presence of secondary phase traces as well as the precise effect of the incorporated dopant, and thus, to clarify the above mentioned contradictions. In this context, the present work pursues a deep and systematic study of the structural and microstructural features of undoped $BiFeO_3$ and WO_3, Nb_2O_5 and TiO_2-modified $BiFeO_3$ ceramics prepared by a solid-state route; a rigorous analysis will let us describe more accurately the effect of these dopants on the microstructure of the $BiFeO_3$ ceramics.

2. Experimental procedures

$BiFeO_3$ (BF), $BiFe_{0.95}W_{0.05}O_3$ (BFW), $BiFe_{0.95}Nb_{0.05}O_3$ (BFN) and $BiFe_{0.95}Ti_{0.05}O_3$ (BFT) ceramics were prepared by a conventional solid-state route. The corresponding amounts of the oxide precursors, Bi_2O_3 (Riedel-de Haën, >99.5%), Fe_2O_3 (Fluka, >99%), WO_3 (Alfa Aesar, >99.8%), Nb_2O_5 (Fluka, >99.5%) and TiO_2 (anatase structure, Titafrance) were weighed and subjected to 2 h of attrition milling with YSZ balls and ethanol as liquid medium. The dried mixtures were sieved under a 100 µm mesh and then thermally treated. Temperatures ranging from 600 to 800 °C with heating and cooling rates of 3 °C/min and soaking times of 2 h were applied. The powders calcined in the optimum conditions were milled and sieved and then pressed isostatically at 200 MPa in $\phi = 0.8$ cm pellets. In order to obtain dense ceramics the pressed pellets were sintered at temperatures between 800 and 900 °C applying heating and cooling rates of 3 °C/min during 2 h.

The calcined powders were characterized by X-ray diffraction to follow the thermal evolution during the $BiFeO_3$ synthesis. The patterns were collected between $2\theta = 15$ and $2\theta = 65°$ on a Bruker D8 Advance diffractometer using CuK_α radiation. The experimental data were refined using the FullProf 2k program [35] and its graphical interface WinPLOTR [36]. Morphological characterization was carried out by Field Emission Scanning Electron Microscopy (FE-SEM) using a Hitachi S-4700 microscope equipped with EDS. Densification behaviour was followed by measuring the Archimedes' density in water. Pellets showing the highest density were structurally characterized by X-ray diffraction. The microstructure of these pellets was also characterized by FESEM-EDS analysis of the polished (with and without chemical etching with dilute HCl) and the fractured surfaces. Micrographs were analyzed using a Leica Q-Win software in order to determinate the grain size.

3. Results and discussion

3.1. Synthesis and characterization

Fig. 1a shows the X-ray diffractograms of the BF calcined powders at different temperatures. As it has been reported earlier [23,37], the solid-state synthesis begins with the formation of the $Bi_{25}FeO_{39}$ sillenite type phase (JCPDS file no.: 00-077-0865) at temperatures below 650 °C. At 750 °C an almost pure $BiFeO_3$ phase is obtained (JCPDS file no.: 01-072-0112). However, traces of the sillenite phase, which will not be further removed, neither by increasing the calcination time nor the temperature, can still be detected. When a small amount of W^{6+} instead of iron is added (BFW sample), the reaction proceeds as in the undoped material and the sillenite-type phase is first formed below 650 °C (Fig. 1b); however this sillenite phase now evolves at 750 °C to form another phase, identified as $Bi_{14}W_2O_{27}$ (JCPDS file no.: 00-039-0061), and this new phase hardly reacts to form $BiFeO_3$ when the temperature is increased. Thus at 800 °C $BiFeO_3$ and $Bi_{14}W_2O_{27}$ are still the major phases detected by XRD, together with some traces of unreacted Fe_2O_3 (JCPDS file no.: 01-079-0007). In the BFN composition the observed reaction pathway is considerably different to that of the undoped sample. At 650 °C a $Bi_2Fe_4O_9$ mullite-type phase (JCPDS file no.: 00-025-0090) is formed together with the sillenite phase (see Fig. 1c). This Fe-rich phase was not detected as a reaction intermediate in the previous BF and BFW compositions, therefore indicating that the presence of Nb^{5+} ions favors its stabilization. When the temperature increases to 700 °C the proportion of the $Bi_2Fe_4O_9$ phase decreases, leading to the formation of another secondary phase with diffraction peaks pointing out to a $A_2B_2O_7$ pyrochlore-type structure [38]. Different studies of the Bi_2O_3–Fe_2O_3–Nb_2O_5 system have made possible describing various Bi–Fe–Nb–O ternary pyrochlores with different stoichiometries [39,40]. In the experimental conditions here used (solid-state under air atmosphere) there is an extended solid-solution region for Bi-deficient pyrochlore stoichiometries in which the Bi^{3+} ions would occupy A positions and the Fe^{3+}, Fe^{2+} and Nb^{5+} ions would be located at B positions of the $A_2B_2O_7$ theoretical formulation [39]. When the temperature is increased up to 750 °C, the concentration of this pyrochlore phase increases at the expense of the $Bi_2Fe_4O_9$

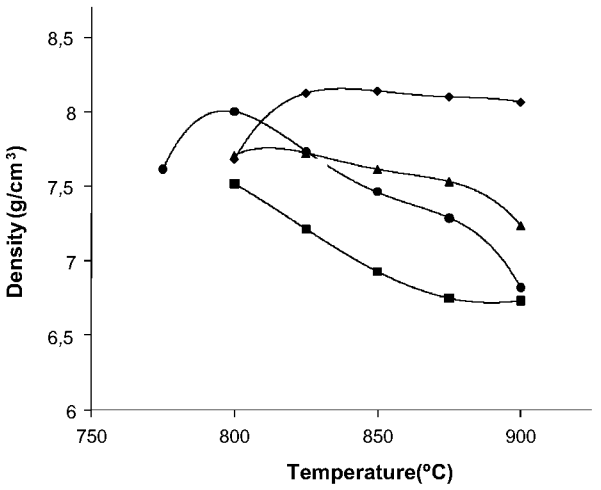

Fig. 3. Archimedes' density (g/cm^3) of the BF (●), BFW (■), BFN (▲) and BFT (♦) materials sintered at different temperatures.

phase, and its presence in a significant amount can still be detected at 800 °C. On the other hand, the thermal evolution of the sillenite-type phase in this BFN sample seems to be the same as in the undoped BF composition: its concentration decreases continuously with temperature while the $BiFeO_3$ phase is being formed. Finally in the case of Ti-doped sample (BFT composition) the reaction pathway is similar to that of the undoped composition, although the reactions occur at slightly higher temperatures (Fig. 1d). Once again the reaction of the $BiFeO_3$ phase is not completed and small amounts of parasitic phases remain in the calcined material, a common feature for all the compositions here prepared by the solid-state synthesis route.

Particle size and morphology of the calcined powders were characterized by FE-SEM. For the undoped composition (BF), a mean particle size of 1 μm is observed, together with the presence of some agglomerates of about 4 μm in size (see Fig. 2a). In the W^{6+}-doped powders a wide particle size distribution is obtained with particle sizes ranging between 300 nm and 1 μm (Fig. 2b). Some dense agglomerates are also observed which indicates that the particles have started to densify. Besides, in this composition particles show different morphologies, spherical and laminar-shaped, probably belonging to different phases. For the BFN composition, a bimodal distribution of the particle size can be inferred (Fig. 2c), with maximums in 500 nm and 1 μm. As in the BFW powders, in BFN there are also some particles with laminar shape, although in this case the overall morphology is more homogeneous. Finally, in the BFT composition the particles are even smaller (Fig. 2d). In this case particle size is about 300 nm and a higher degree of homogeneity is achieved. Moreover, the morphology of the particles is more spherical and homogeneous than in the undoped or the W^{6+} or Nb^{5+}-doped samples.

3.2. Sintering behaviour

Fig. 3 shows the evolution of density as a function of temperature for the BF, BFW, BFN and BFT materials. In the undoped (BF) material, the maximum value of density is reached at 800 °C. At this temperature, a density of 8.00 ± 0.05 g/cm^3 is obtained, which corresponds to the 95.4% of the theoretical density of $BiFeO_3$ (8.416 g/cm^3; JCPDS file no.: 01-072-0112). In the BFW composition, the densification is lower. When sintering at 800 °C a maximum density of 7.52 ± 0.05 g/cm^3 is achieved. The density of the pellets suddenly decreases at higher temperatures and this might be due to an increasing proportion of $Bi_2Fe_4O_9$ phase which shows a theoretical density of $\rho = 6.473$ g/cm^3, significantly lower

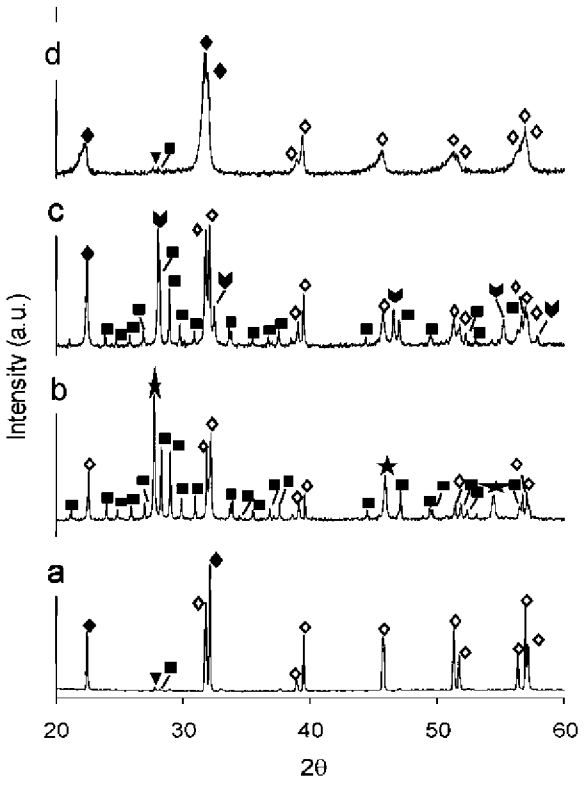

Fig. 4. X-ray diffractograms of the BF (a), BFW (b), BFN (c) and BFT (d) materials sintered at the temperature of higher densification. $BiFeO_3$ (♦), $Bi_{25}FeO_{39}$ (▼), $Bi_2Fe_4O_9$ (■), $Bi_{14}W_2O_{27}$ (★), and $Bi_{1.70}Nb_{0.30}O_{3.30}$ (⮟).

than that of $BiFeO_3$, ($\rho = 8.416$ g/cm^3). When sintering above 850 °C the pellets melted. Taking into account the phases present in the calcined BFW powders, this situation may be ascribed to the presence of the $Bi_{14}W_2O_{14}$ phase, which starts melting around 850 °C [41]. With the Nb-doping (BFN composition) the maximum density is closer to that of the undoped pellets, 7.72 ± 0.05 g/cm^3, although it is achieved at the slightly higher temperature of 825 °C. The percentage of theoretical density for each of these materials – calculated from the rough phase proportion showed in the XRD (Fig. 4b and c) – is about 93% for the BFW material sintered at 800 °C (theoretical density ≅8.08 g/cm^3) and about 97% for the BFN material sintered at 825 °C (theoretical density ≅8.05 g/cm^3). As in the BFW composition, the density decreases when increasing temperature, resulting from the increasing proportion of $Bi_2Fe_4O_9$ secondary phase. Finally, doping with Ti^{4+} gives raise to an enhancement in the densification. In this case a density of 8.13 ± 0.05 g/cm^3, 97.1% of the $BiFeO_3$ theoretical density, is reached at 825 °C, a much higher value than for the undoped composition. The density values are now more stable and hardly decrease with increasing sintering temperature (see Fig. 3) since there is almost no phase evolution and no noticeable grain growth [42].

3.3. Microstructure characterization

Fig. 4 shows the XRD results of the samples of each composition sintered at the temperatures of their higher densification. In the case of BF and BFT compositions an almost $BiFeO_3$ pure phase is obtained (Fig. 4a and d respectively) although, similarly to what happened with the calcined powders, traces of the $Bi_{25}FeO_{39}$ and $Bi_2Fe_4O_9$ phases can be inferred for both compositions. In the case of both BFW and BFN compositions, the proportion of secondary phases is even higher than in the calcined powders. In the W^{6+} doped ceramics (Fig. 4b) the $Bi_{12}W_2O_{27}$ secondary phase

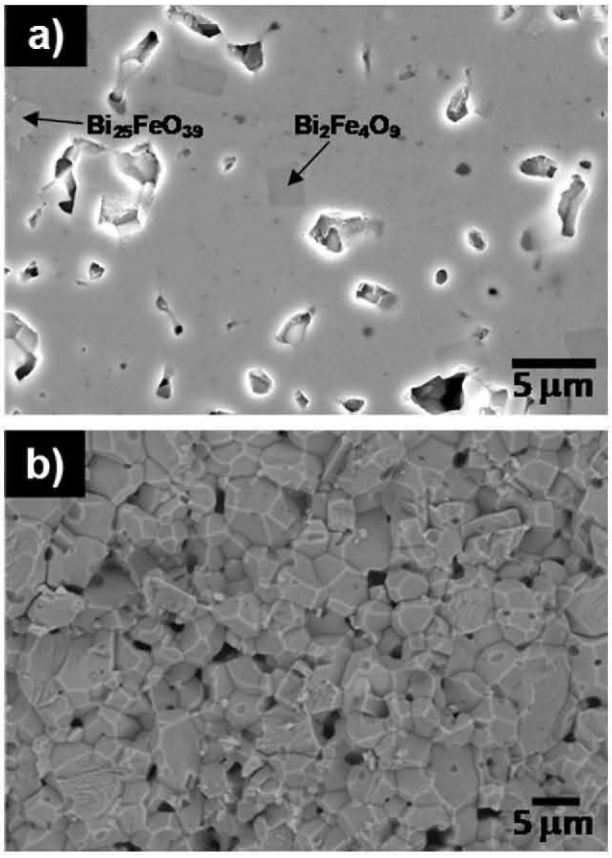

Fig. 5. FE-SEM micrographs of the BF material on the polished surface (a) and on the fracture surface (b). The secondary phases identified by the EDS analysis are marked on the micrograph (a); the matrix corresponds to the $BiFeO_3$ phase.

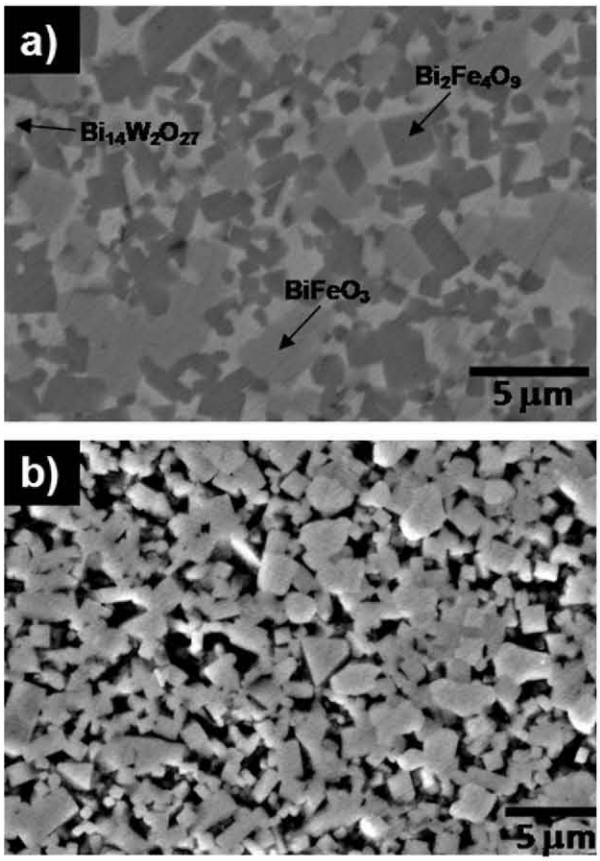

Fig. 6. FE-SEM micrographs of the BFW material on the polished surface (a) and on the etched polished surface (b). The phases identified by the EDS analysis are marked on the micrograph (a).

increases its concentration upon heating, being the main phase in the sintered material. The unreacted Fe_2O_3 phase does not appear after sintering and, instead, a considerable amount the mullite type phase ($Bi_2Fe_4O_9$) is now obtained as an iron rich secondary phase. For the BFN material a parallel situation takes place and high amounts of secondary phases appear in the sintered samples: although $BiFeO_3$ is still the major phase, strong signals of a Bi–Nb phase, $Bi_{1.70}Nb_{0.30}O_{3.30}$ (JCPDS file no.: 00-33-0210), and the Fe-rich $Bi_2Fe_4O_9$ phase are now present (Fig. 4c). The sillenite and the pyrochlore-type phases that were present as traces in the calcined powder are, however, not detected in the sintered material. These results certainly indicate that the sillenite and the Bi–Fe–Nb–O pyrochlore react during sintering, giving rise to the formation of a high amount of $Bi_2Fe_4O_9$ and a bismuth–niobium double oxide. In view of these results, only titanium-doping seems to stabilize the $BiFeO_3$ structure, while tungsten or niobium-doping stabilize different secondary phases (similar behaviour to what has been reported for some other common impurities like SiO_2 or Al_2O_3 [16]). Furthermore, the X-ray diffractograms of the titanium doped materials (BFT) also show a noticeable displacement of the $BiFeO_3$ broadened diffraction peaks (Fig. 4d). The cell parameters calculated for the BFT materials sintered at 825 °C are $a = b = 5.582(5)$ Å and $c = 13.86(1)$ Å, whereas those for the undoped $BiFeO_3$ are $a = b = 5.576(3)$ Å and $c = 13.863(8)$ Å; this means an increase in the unit cell volume from 373.310 Å^3 in the undoped BF system to 374.128 Å^3 in the Ti-doped one. Such an increase may result from the balance between two different effects: on one hand Ti^{4+} ions are smaller than Fe^{3+} ions (0.605 and 0.645 Å respectively [33]), so substitution of Fe^{3+} for Ti^{4+} should cause a decrease in the lattice constants. On the other hand, in order to compensate the charge mismatch, such substitution may as well imply a diminution in the oxygen vacancies concentration, therefore leading to an increase in the lattice constant. The experimental values hence indicate that suppression of oxygen vacancies prevails over the differences in ionic radii. This possibility will be discussed later but, at this point, the observed changes in the cell parameters certainly indicate that Ti^{4+} is entering the perovskite structure, explaining why no Ti-additional secondary phases are formed within this doped composition.

Fig. 5a shows a micrograph of the polished surface of BF sample sintered at 800 °C. The EDS analysis carried out on the light-grey matrix indicated a Bi/Fe ratio ≅1, confirming that we are dealing with the $BiFeO_3$ phase. In addition the square dark-grey grains were identified as the $Bi_2Fe_4O_9$ phase, while the bright and irregularly shaped grains belong to the Bi-rich sillenite phase as determined by EDS. The size of the $BiFeO_3$ matrix grains was measured from the micrographs of the fractured surface (Fig. 5b) yielding an average size of 3 μm.

Fig. 6a shows the microstructure of the polished surface of the BFW sample sintered at 800 °C. EDS analysis were used to identify the different phases. The square darker grains correspond to the $Bi_2Fe_4O_9$ phase, but now the brightest areas showed a Bi/W ratio of approximately 7 which may be ascribed to the $Bi_{14}W_2O_{27}$ phase that was identified by XRD measurements. The $BiFeO_3$ phase appears as big grey areas in the micrograph. The analysis of the etched region (Fig. 6b) shows $BiFeO_3$ grains with a bimodal distribution and maximums of 1 and 2 μm; the square $Bi_2Fe_4O_9$ grains exhibit an average size of 1 μm. The EDS analysis confirmed the Bi/Fe ratio being close to 1, with no W detected in these areas. Somehow this result was expected from the previous XRD characterization: the high reactivity between bismuth and tungsten

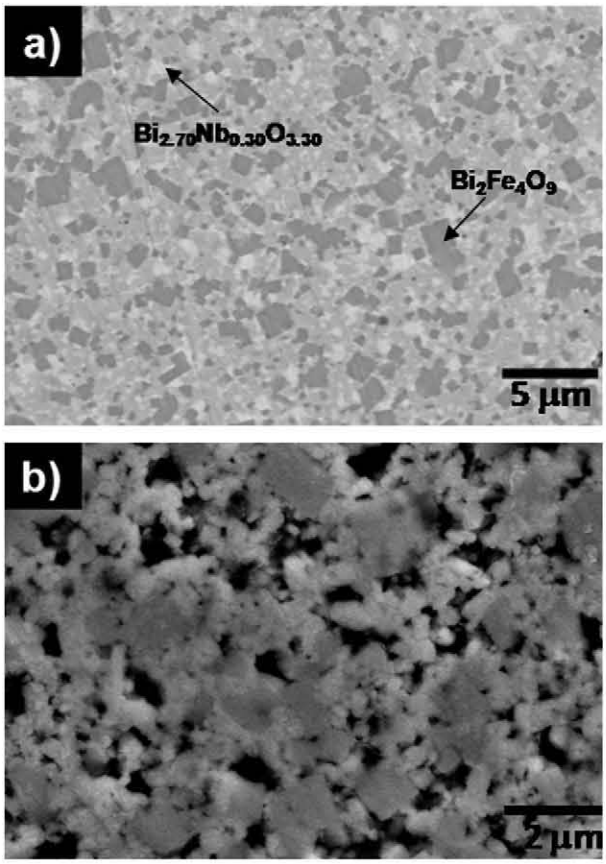

Fig. 7. FE-SEM micrographs of the BFN material on the polished surface (a) and on the etched polished surface (b). The secondary phases identified by the EDS analysis are marked on the micrograph (a); the matrix corresponds to the $BiFeO_3$ phase.

preferentially leads to the formation of Bi–W-based phases and these phases confine the W^{6+} ions, thus avoiding their incorporation into the $BiFeO_3$ perovskite structure.

Micrographs of the BFN pellets sintered at their maximum densification temperature are shown in Fig. 7. A high proportion of secondary phases are observed in the microstructure, although not as high as in the W-doped composition. The $Bi_2Fe_4O_9$ phase appears once again as dark square grains distributed throughout the entire sample. In the non etched region (Fig. 7a) some dispersed big bright spots are observed. These regions were identified as a Bi-rich phase containing niobium by the semi-quantitative EDS analysis. Moreover, the EDS showed that the niobium added to the composition is mainly located in this Bi-rich secondary phase, not being detected in other phases. On the other hand, the micrograph on the etched surface (Fig. 7b) shows a $BiFeO_3$ grain size around 500 nm, much smaller than in the undoped composition. In both BFN and BFW compositions the dopant is incorporated into the Bi-rich secondary phases rather than in the $BiFeO_3$ perovskite structure; the observed reduction in grain size as compared to the undoped sample could then be attributed to a slow diffusion process caused by the continuous formation/decomposition reactions between different secondary phases, but also to a pinning effect exerted by smaller particles (probably remains of the sillenite or the pyrochlore-type phases).

Fig. 8 shows the FESEM micrographs of the polished surface of BFT pellets sintered at 825 °C. EDS allowed the identification of the $BiFeO_3$ major phase but also the secondary phases that were hidden to the X-ray diffraction analysis. These secondary phases are those that usually appear in the Bi_2O_3–Fe_2O_3 system: the mullite $Bi_2Fe_4O_9$ (square dark-grey grains) and the sillenite $Bi_{25}FeO_{39}$

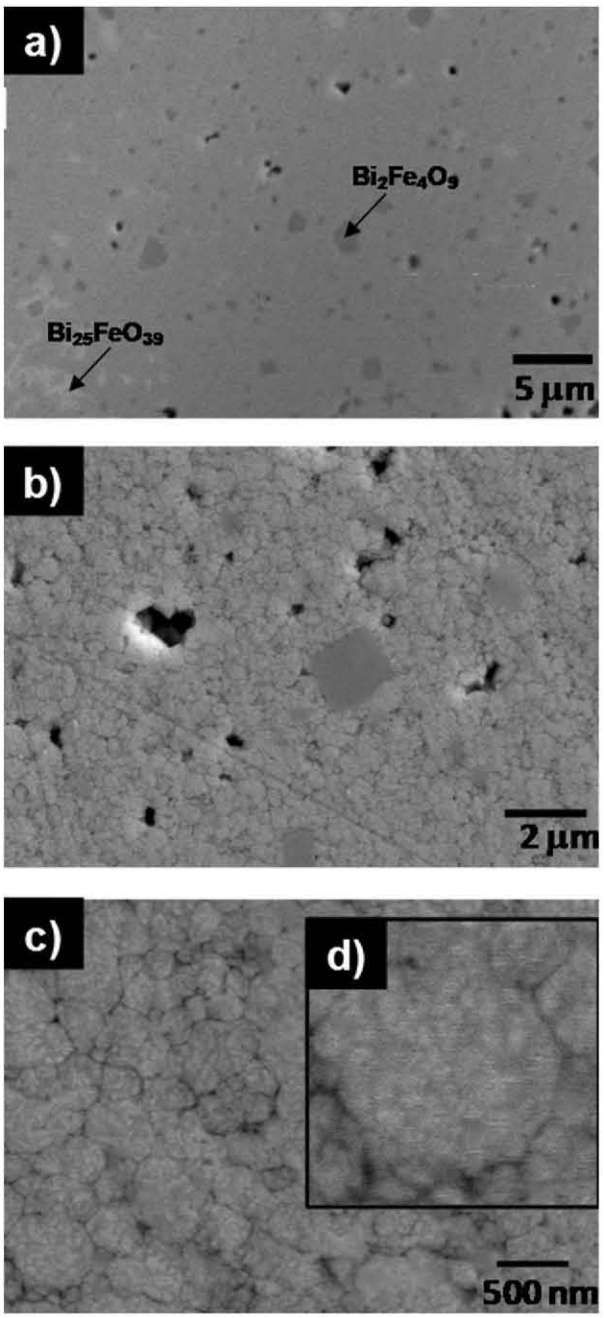

Fig. 8. FE-SEM micrographs of the BF material on the polished surface (a) and on the polished and etched surface (b and c). The inset (d) shows a zoom-in of a $BiFeO_3$ grain nanostructure. The secondary phases identified by the EDS analysis are marked on the micrograph (a); the matrix corresponds to the $BiFeO_3$ phase.

(small and dispersed bright spots). The image-analysis also showed that the proportion of secondary phases in this BFT composition is slightly smaller than in the undoped material and certainly much smaller than in the W- or Nb-doped systems. Moreover, EDS measurements showed that the added titanium is only present in the $BiFeO_3$ grains, not being detected in the other phases. This confirms that, as inferred from the XRD characterization analyses, Ti^{4+} ions enter the perovskite structure and play a key role in the stabilization of this $BiFeO_3$ phase, decreasing the proportion of secondary phases. Regarding grain size, micrographs of the etched surface (Fig. 8b and c) reveal a very homogeneous microstructure in which the matrix grains of $BiFeO_3$ now exhibit an average size of 0.5 µm. A more detailed analysis of the microstructure allowed the obser-

vation of a nanostructure of around 50 nm inside the $BiFeO_3$ grains (see inset of Fig. 8d). A clear description of the precise nature of this nanostructure requires further characterization (currently in progress), but up to now there is something noteworthy at this point. That mean grain size of 50 nm deduced from the FESEM image is in agreement with that of the crystal size estimated using Scherrer's equation from the XRD spectrum of this sintered sample (Fig. 4d), which yields approximately 40 nm; furthermore, a similar value is also obtained if we estimate the crystal size of the calcined powders of this composition. This implies that there is almost no grain growth during the sintering step of this particular composition (at least at the temperatures of its maximum densification). Consequently, this material exhibits the highest density and the lowest grain size of all tested compositions, including the undoped one, and this fact must be attributed to the presence of Ti^{4+} ions inside the perovskite structure: since they have a higher valence than Fe^{3+} ions, these Ti^{4+} ions will act like donors and thus they will suppress some oxygen vacancies defects. More specifically, the reactions can be described in terms of the Krogen–Vink notation as follows:

$$Bi_2O_3 + 2TiO_2 \rightarrow 2(Bi_{Bi})^X + 2(Ti_{Fe})^{\bullet} + 6O_O{}^X + \tfrac{1}{2}O_2 + 2e^- \quad (1)$$

$$\tfrac{1}{2}O_2 + V_O{}^{\bullet\bullet} + 2e^- \rightarrow O_O{}^X \quad (2)$$

As it is well known, the suppression of oxygen vacancies restrains the diffusion of matter that leads to grain growth [43], thus contributing to a reduced grain size. Besides, incorporation of the Ti^{4+} ions into the $BiFeO_3$ grains may as well cause solute-drag effect, which also helps control grain size [44]. The fact is both effects lead to a smaller grain size than in the undoped samples and, at the same time, explain why we obtained a better densification trend in this Ti-doped composition (see Fig. 3).

4. Conclusions

The results obtained in the present work show that the addition of W^{6+} or Nb^{5+} to $BiFeO_3$ bulk ceramics modifies the solid state formation of the $BiFeO_3$ phase, which takes place through different intermediate phases. As a consequence, materials with high proportion of secondary phases that confine the added W^{6+} or Nb^{5+} dopants are obtained. On the other hand, the addition of Ti^{4+} ions leads to dense nanostructured ceramics with an exceptionally low proportion of secondary phases (practically undetectable by XRD) which has never been obtained through a solid state synthesis process. The EDS analysis reveals that the added titanium enters the perovskite structure of $BiFeO_3$ and reduces the formation of secondary phases. Therefore, it is possible to stabilize the $BiFeO_3$ phase by doping with titanium. In addition, Ti-doping leads to a grain growth control which can be explained from the point of view of defects chemistry.

Acknowledgements

This work has been conducted within the CICYT MAT 2010-16614 project. M.S. Bernardo also acknowledges the Spanish Ministry of Education for the financial support (FPU scholarship program).

References

[1] N.A. Spaldin, M. Fiebig, Science 309 (2005) 391–392.
[2] W. Eerenstein, N.D. Mathur, J.F. Scott, Nature 442 (2006) 759–765.
[3] G. Catalan, J.F. Scott, Adv. Mater. 21 (2009) 2463–2485.
[4] W.N. Su, D.H. Wang, Q.Q. Cao, Z.D. Han, J. Yin, J.R. Zhang, Y.W. Du, Appl. Phys. Lett. 91 (2007) 092905.
[5] H. Ke, W. Wang, Y. Wang, J. Xu, D. Jia, Z. Lu, Y. Zhou, J. Alloys Compd. 509 (2011) 2192–2197.
[6] J.H. Xu, H. Ke, D.C. Jia, W. Wang, Y. Zhou, J. Alloys Compd. 472 (2009) 473–477.
[7] K. Wajcik, T. Raffer, H. Lang, A.A. Auer, M. Mehring, J. Organomet. Chem. 696 (2011) 1647–1651.
[8] J.L. Mi, T.N. Jensen, M. Christensen, C. Tyrsted, J.E. Jargensen, B.B. Iversen, Chem. Mater. 23 (2011) 1158–1165.
[9] S.H. Han, K.S. Kim, H.G. Kim, H.G. Lee, H.W. Kang, J.S. Kim, C.I. Cheon, Ceram. Int. 36 (2010) 1365–1372.
[10] D. Maurya, H. Thota, K.S. Nalwa, A. Garg, J. Alloys Compd. 477 (2009) 780–784.
[11] J. Prado-Gonjal, M.E. Villafuerte-Castrejón, L. Fuentes, E. Morán, Mater. Res. Bull. 44 (2009) 1734–1737.
[12] Farhadi, Saeid, Rashidi, Nazanin, J. Alloys Compd. 503 (2010) 439–444.
[13] J. Chen, X. Xing, A. Watson, W. Wang, R. Yu, J. Deng, L. Yan, C. Sun, X. Chen, Chem. Mater. 19 (2007) 3598–3600.
[14] T.T. Carvalho, P.B. Tavares, Mater. Lett. 62 (2008) 3984–3986.
[15] S.M. Selbach, M.A. Einarsrud, T. Grande, Chem. Mater. 21 (2009) 169–173.
[16] M. Valant, A.K. Axelsson, N. Alford, Chem. Mater. 19 (2007) 5431–5436.
[17] A.Z. Simões, F.G. Garcia, C.S. Riccardi, Mater. Chem. Phys. 116 (2009) 305–309.
[18] A. Ianculescu, F.P. Gheorghiu, P. Postolache, O. Oprea, L. Mitoseriu, J. Alloys Compd. 504 (2010) 420–426.
[19] N.V. Minh, D.V. Thang, J. Alloys Compd. 505 (2010) 619–622.
[20] N.V. Minh, N.G. Quan, J. Alloys Compd. 509 (2011) 2663–2666.
[21] Z. Zhang, P. Wu, L. Chen, J. Wang, Appl. Phys. Lett. 96 (23) (2010) 232906.
[22] X. Qi, J. Dho, R. Tomov, M.G. Blamire, J.L. MacManus-Driscoll, Appl. Phys. Lett. 86 (2005) 062903.
[23] M.S. Bernardo, T. Jardiel, M. Villegas, Bol. Soc. Esp. Ceram. V 49 (2010) 47–52.
[24] F. Azough, R. Freer, M. Thrall, R. Cernik, F. Tuna, D. Collison, J. Eur. Ceram. Soc. 30 (2009) 727–736.
[25] Y.H. Guet, et al., J. Appl. Phys. 108 (9) (2010) 094112.
[26] M. Kumar, K.L. Yadav, J. Appl. Phys. 100 (2006) 074111.
[27] Y. Wang, C.W. Nan, Appl. Phys. Lett. 89 (2006) 052903.
[28] Y.K. Jun, W.T. Moon, C.M. Chang, H.S. Kim, H.S. Ryu, J.W. Kim, K.H. Kim, S.H. Hong, Solid State Commun. 135 (2005) 133–137.
[29] Y.K. Jun, S.H. Hong, Solid State Commun. 144 (2007) 329–333.
[30] A.Z. Simões, R.F. Pianno, E.C. Aguiar, E. Longo, J.A. Varela, J. Alloys Compd. 479 (2009) 274–279.
[31] A.Z. Simões, F.G. Garcia, C.S. Riccardi, J. Alloys Compd. 493 (2010) 158–162.
[32] L. Cheng, G. Hu, B. Jiang, C. Yang, W. Wu, S. Fan, Appl. Phys. Express 3 (2010) 101501.
[33] R.D. Shannon, Acta Crystallogr. A 32 (1976) 751–767.
[34] I.S. Lyubutin, A.G. Gavriliuk, V.V. Struzhkin, JETP Lett. 88 (2008) 524–530.
[35] T. Roisnel, J. Rodriguez-Carjaval, FULLPROF Phys. B 192 (1993) 55, See also http://www-llb.cea.fr/fullweb/fp2k/fp2k.htm.
[36] T. Roisnel, J. Rodríguez-Carvajal, Proc. of the 7th European Powder Diffraction Conference (EPDIC 7), R. Delhez, E.J. Mittenmeijer (Eds.) (2000) 118. See also http://www-llb.cea.fr/fullweb/winplotr/winplotr.htm.
[37] M.S. Bernardo, T. Jardiel, M. Peiteado, A.C. Caballero, M. Villegas, doi:10.1016/j.jeurceramsoc.2011.03.018.
[38] M. Peiteado, M.A. De La Rubia, J.F. Fernández, A.C. Caballero, J. Mater. Sci. 41 (2006) 2319–2325.
[39] M.W. Lufaso, T.A. Vanderah, I.M. Pazos, I. Levin, R.S. Roth, J.C. Nino, V. Provenzano, P.K. Schenck, J. Solid State Chem. 179 (2006) 3900–3910.
[40] I.E. Grey, W.G. Mumme, T.A. Vanderah, R.S. Roth, C. Bougerol, J. Solid State Chem. 180 (2007) 158–166.
[41] S.N. Hoda, L.L.Y. Chang, J. Am. Ceram. Soc. 57 (7) (1974) 323–326.
[42] M.N. Rahamn, Ceramic Procesing and sintering (2nd. Ed.), Marcel Dekker, New York, 1995.
[43] H.M. Chan, M.P. Harmer, D.M. Smyth, J. Am. Ceram. Soc. 69 (6) (1986) 507–510.
[44] T. Jardiel, M.A. De la Rubia, M. Peiteado, J. Am. Ceram. Soc. 91 (2008) 1083–1087.